Title: Highly NIR-II Scattering Gold Superclusters for Intravascular Optical Coherence Tomography Molecular Imaging

Authors: Nicholas D. Calvert [1], Joshua Baxter [2], Aidan A. Torrens [1], Jesse Thompson [2], Alexia Kirby [3], Jaspreet Walia [4], Spyridon Ntais[4], Eva Hemmer [1], Pierre Berini [2,4], Benjamin Hibbert [5], Lora Ramunno [2], Adam J. Shuhendler [1, 3, 5*]

*Corresponding Author: adam.shuhendler@uottawa.ca

Affiliations:

[1]Department of Chemistry and Biomolecular Sciences, University of Ottawa, 150 Louis Pasteur Pvt., Ottawa, Ontario, Canada, K1N 6N5

[2]Department of Physics, University of Ottawa, 150 Louis Pasteur Pvt., Ottawa, Ontario, Canada, K1N 6N5

[3]Department of Biology, University of Ottawa, 150 Louis Pasteur Pvt., Ottawa, Ontario, Canada, K1N 6N5

[4]School of Electrical Engineering and Computer Science, University of Ottawa, 800 King Edward Ave., Ottawa, Ontario, Canada, K1N 6N5

[5]University of Ottawa Heart Institute, 40 Ruskin St., Ottawa, Ontario, Canada, K1Y 4W7

Abstract:

In North America, intravascular optical coherence tomography (IV-OCT) is performed every few minutes to evaluate atherosclerotic plaques and guide stent placement. Currently, IV-OCT is limited to anatomical imaging, providing structural information about atherosclerotic plaque morphology, thrombus, and dissection. Earlier detection and risk stratification would be possible through molecular characterization of endothelium but necessitates a purpose-engineered IV-OCT contrast agent. We developed gold superclusters (AuSC) tailored to clinical instrumentation and integrated into clinically relevant workflows. AuSC are aqueously dispersible clusters of closely packed small gold nanoparticles, affording plasmon hybridization to maximize light scattering at the IV-OCT laser line (~1350 nm). A polymer coating fosters AuSC uniformity and provides a functionalizable handle, which we targeted to intravascular P-selectin, an early vascular endothelial marker of inflammation. In a rat model of intravascular inflammation, P-selectin-targeted AuSC facilitated IV-OCT molecular imaging, where the strength of the signal correlates with the severity of vascular inflammation. AuSC thus enable *in vivo* molecular imaging, advancing IV-OCT into the molecular age.

Main:

Recently, optical biomedical imaging techniques have focused on harnessing photobiophysical interactions in the second near-infrared window (NIR-II, 900 nm – 1700 nm).[1,2] This focus is a result of the unique interaction of incident and emitted NIR-II photons with tissue: minimized light scattering, reduced tissue autofluorescence, and deeper light penetration.[1–3] Extensive research effort has been dedicated to developing biocompatible molecules and materials that are active in the NIR-II region[4–7]. Plasmonic nanomaterials are of special interest due to the tunability of their localized surface plasmon resonance (LSPR) properties, allowing photobiophysical interactions to occur across the visible and NIR spectrum.[8–10] To date, there has been limited innovation in contrast agents for optical coherence tomography (OCT), which is among the most predominant clinical NIR-II imaging technologies.

OCT is primarily used for ocular and intravascular (IV) procedures, where images are created by destructive or constructive interference in backscattered NIR-II light from a laser source relative to a reference mirror.[11–13] IV-OCT is performed using an imaging catheter inserted into the patient's radial or femoral artery, and routed to the aortic vasculature.[14] A rotating NIR-II light source in the catheter is attached to a camera that, upon pull-back, generates a three-dimensional image of the vascular region. IV-OCT is growing in clinical popularity, with procedures being performed every few minutes in the United States,[15] but is limited to providing clinicians with anatomical information about diseased arteries or placed stents.[16] Molecular imaging-guided IV-OCT would allow physicians to extend their evaluation of vascular pathology beyond just anatomical, providing the identification of molecular markers of disease that appear much earlier in disease progression than anatomical changes. Molecular imaging can also provide information not otherwise accessible, such as identifying early biomarkers of plaques that may rupture as an alternative to current stratification by anatomic plaque features. This would allow physicians to better risk-stratify their patient population.[17,18] A purpose-engineered contrast agent for IV-OCT would justify the use of IV-OCT in almost 7 million more cardiovascular cases in the United States *per* year.[15]

An ideal purpose-built contrast agent for IV-OCT would induce destructive interference (*i.e.*, scattering) of the incident laser light once immobilized by a molecular binding event, resulting in image contrast features within the black vascular lumen. Such contrast agents could be comprised of plasmonic metals, supporting LSPR within the NIR-II region.[19] However, current agents for NIR-II LSPR are often composed of bioactive metals such as Cu or Ag, making them suboptimal for biomedical use.[20–22] Gold nanoparticles (AuNPs), commonly used in a range of biomedical imaging techniques,[23,24] have also been evaluated for OCT.[25,26] Rods and other non-spherical shapes have been shown to support NIR-II LSPRs, but these shapes do not clear the body as effectively as their spherical counterpart, which is an important consideration

for intravascular applications.[27] Gold nanoshells have been shown to have excellent NIR-II interactions and have been shown as effective contrast agent in *in vitro* OCT work.[28–31] In addition to NIR-II LSPR and clearance characteristics, an ideal IV-OCT contrast agent enabling molecular imaging would be able to signal relatively rare instances of expression of its biomolecular target. By nature, IV-OCT is dynamic since the imaging catheter is pulled through the vessel to acquire the image. As a result, limited sensor dwell time makes the acquisition of molecular information by IV-OCT challenging. We hypothesize that this challenge can be met with a large contrast agent that fills a larger portion of a voxel, preventing the averaging out of signal within a voxel. In consideration of these performance and materials requirements, there is no instance of a purpose-designed, spherical contrast agent for IV-OCT.

To date, only a single report could be found on the synthesis of gold superclusters interacting with NIR-II light, but which resulted in highly heterogeneously shaped constructs (spheres and networks of fused spheres) that were not aqueously dispersible.[32] Recently, a synthesis of *in vivo* disassembling gold supraclusters was reported,[33] but this ionic assembly was designed to aggregate within the low pH of intratumoral environments and disassemble at physiological pH. While elegant, the resulting AuNP assembly precludes plasmon hybridization, abolishing NIR-II interactions and preventing its use as an IV-OCT contrast agent.

In this study, we report the synthesis of uniform, aqueously dispersible gold superclusters (AuSC) as IV-OCT contrast agents, having ideal characteristics for molecular imaging. We have achieved controlled aggregation of oleylamine-capped AuNPs by varying solvent polarity and have also stabilized AuSC by “cinching” them with large amphiphilic polymers. This polymer coating enables stable aqueous dispersion of AuSC in isotonic media, resulting in biologically relevant supercluster materials. Our solvothermally-driven, one-pot *in situ* nucleation and clustering synthesis approach produces AuSC of unique architecture, supporting a LSPR peak in the NIR-II region that is almost entirely scattering. Furthermore, we have demonstrated the ability to functionalize the stabilizing polymers by attaching biomolecular targeting moieties without sacrificing the physicochemical properties that make AuSC an attractive IV-OCT molecular imaging agent. We functionalized AuSC with a P-selectin ligand mimic to facilitate AuSC binding to highly inflammatory regions of endovasculature with pathology-associated protein expression preceding anatomical changes in the tissue. Finally, using a clinical IV-OCT instrument and imaging catheter, we mapped intravascular inflammation stimulated by *intravenous (iv)* lipopolysaccharide (LPS) injection in rats, thereby demonstrating *in vivo* molecular imaging with IV-OCT.

Synthesis and characterization of aqueously dispersible, NIR-II scattering gold superclusters (AuSC@(Myrj52)$_2$):

In engineering AuSC suitable for *in vivo* imaging, a scalable synthetic method with high batch-to-batch reproducibility was sought. Drawing inspiration from oleylamine capped AuNP clustering initiated by the reduction of $HAuCl_4$ by ethylene glycol through heating,[32] we developed a rapid (~ 5 min) one-pot microwave-assisted method instead of following the more traditional oil bath heating approach. This microwave-assisted method ensured a more homogeneous heating in order to better convert $HAuCl_4$ into AuSCs. Synthetic parameters, including the concentration of gold precursor and capping agents, reaction temperature, and reaction times, were optimized to generate spherical and uniform clusters (Supplementary Table 1). In this work, oleylamine was the chosen capping agent throughout. The most critical parameter for AuSC formation from $HAuCl_4$ was the solvophobic effect, controlled by the polarity of the dispersion solvent. Highly polar solvents, such as methanol, induced tight, branching clusters, whereas highly non-polar solvents, such as hexanes, lacked the proclustering driving force necessary for AuSC formation, and instead yielded discrete AuNPs (Fig. 1).

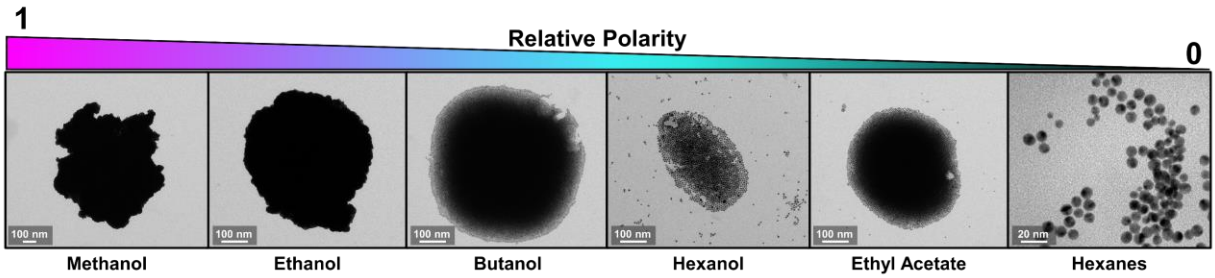

Figure 1. Effect of solvent polarity on oleylamine-capped AuNP clustering. Oleylamine-capped AuNPs following microwave synthesis were redispersed in solvents of varying relative polarities, then imaged by TEM.

Of the solvents tested, *n*-butanol generated the most homogenously spherical AuSC (Fig 1) and was used as the solvent for the proclustering step in our AuSC synthesis (Fig. 2A). However, as synthesized, bare AuSC were unstable under electron microscopy, as individual AuNPs were seen disassembling at the AuSC edges (Fig. 2B, C, left panel) and the nanotopography[34] appearing flat and collapsed (Fig. 2D, left panel). These AuSC gave a very broad LSPR peak centered at ~1000 nm (Fig. 2E, black curve), with a highly heterogeneous size and shape distribution of median diameter (d) = 181.1 nm (interquartile range [IQR]: 74 – 403 nm) (Fig. 2F, black bars). AuSC stabilization was achieved using amphiphilic polymers, containing a long aliphatic chain to interact with the hydrophobic oleylamine coating of the AuNPs, and a long hydrophilic portion to interact with aqueous solvents. Many different polymers were tested, with a comprehensive account of their effects on AuSC physicochemical properties shown in Supplementary Fig. 1. While all tested polymers performed

similarly, ultimately, polyethylene oxide (40) stearate (Myrj52) was chosen for ease of downstream chemical functionalization, and for its known biocompatibility.[35,36] To achieve the polymer coating, AuSC were mixed in an *n*-butanol solution of Myrj52 to form AuSC@(Myrj52) (Fig. 2A, center panel). Qualitatively, AuSC@(Myrj52) had much tighter intraparticle spacing between the individual AuNPs (Fig. 2B, C, center panel), and appeared more spherical than bare AuSC (Fig. 2D, center *vs.* left panels). The resulting LSPR peak was narrower than in bare AuSC, centered at ~1100 nm (Fig. 2E, orange curve). The observed peak narrowing can be attributed to the narrower size distribution of AuSC@(Myrj52) following stabilization (d = 216 nm (IQR: 79 – 477 nm), Fig. 2F, orange bars). Despite improvement in nanotopography and optical properties, AuSC@(Myrj52) were still not dispersible in water. We hypothesized that a highly concentrated aqueous solution of Myrj52 could be used to further coat AuSC@(Myrj52) through polymer-polymer interactions, which resulted in aqueously dispersible AuSC@(Myrj52)$_2$ (Fig. 2A, right panel). AuNP packing appeared tighter in AuSC@(Myrj52)$_2$ compared to AuSC@(Myrj52) (Fig. 2B, C, middle *vs.* right panel), and the overall cluster population appeared more homogeneous and with a more spherical nanotopography (Fig. 2D, right panel). After removal from the polymer solution and their dispersion in water, AuSC@(Myrj52)$_2$ displayed a narrower LSPR peak centered ~1350 nm (Fig. 2E, blue curve), attributable to the homogeneous population of AuSC@(Myrj52)$_2$, with d = 419 nm (IQR: 326 – 485 nm) (Fig. 2F, blue bars). An extended LSPR spectra of AuSC@(Myrj52) in *n*-butanol can be seen in Supplementary Fig. 2. Synthesis of AuSC@(Myrj52)$_2$ using 0.9% $NaCl_{(aq)}$ (saline) for the aqueous transfer steps was evaluated and no effect of the isotonic solution on cluster morphology or physicochemical properties was observed (Supplementary Fig. 3).

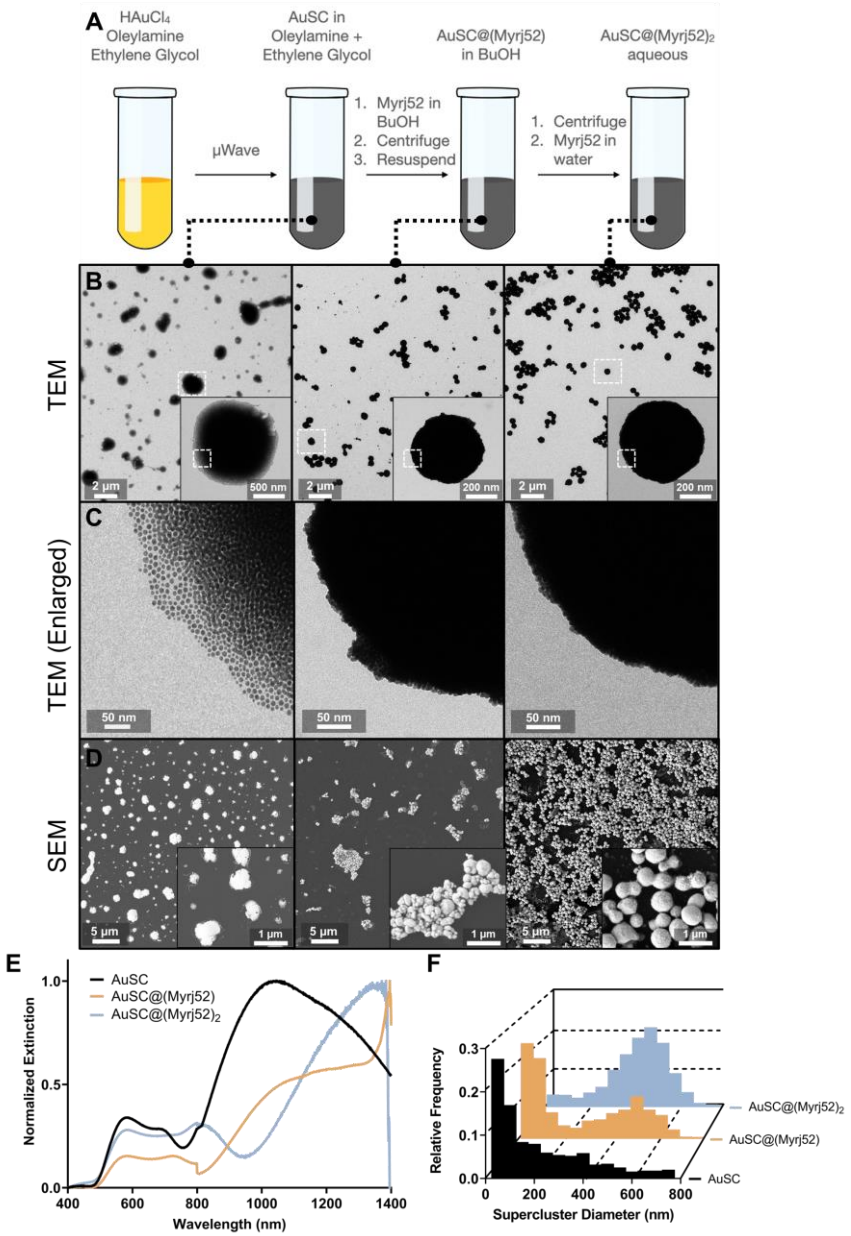

Figure 2. Optimized synthesis of AuSC and their physicochemical properties. A) Illustration of the optimized one-pot solvothermal synthetic method, proceeding from $HAuCl_4$ to water-dispersible AuSC (AuSC@(Myrj52)$_2$). B) Transmission electron microscopy images of AuSC after each synthetic step. White boxes in the primary image are magnified in the bottom right corner. White boxes in these magnified images are further magnified in C). D) Scanning electron microscopy images after each synthetic step. Images in the bottom right corner are magnified from the main image. E) Extinction spectra of AuSC after each synthetic step. The spectra for AuSC and AuSC@(Myrj52) were acquired in *n*-butanol, while that of AuSC@(Myrj52)$_2$ was acquired in water. F) Binned relative frequency of cluster diameters derived from two independent AuSC syntheses and extracted from TEM (n = 1015 (black), 1455 (orange), and 5041 clusters (blue)).

Stabilized intraparticle interactions induce NIR-II redshifting of AuSCs through global plasmon hybridization:

Plasmon hybridization of AuNPs is well-studied,[37,38] but a persistent hybridization of many AuNPs, as present in the AuSC reported here, has yet to be observed or evaluated. Initial calculations were based on the median diameter (d) of AuNPs comprising AuSCs, determined by disassembly of water dispersed AuSC@$(Myrj52)_2$ by addition of a large volume of hexanes and overnight sonication. A significant input of energy in the form of sonication was necessary for AuSC disassembly. AuNPs from disassembled AuSC@$(Myrj52)_2$ (Fig. 3A, left panel) showed a homogeneous population of median d = 9 nm (IQR 8 – 10 nm, $AuNP_9$, Fig. 3A, center panel). Based on this median d, a single AuSC@$(Myrj52)_2$ cluster was calculated to contain ~1×10^9 AuNPs. The large number of AuNPs that comprised AuSC@$(Myrj52)_2$ led us to refer to the LSPR interaction occurring between all AuNPs within the as Global Plasmon Hybridization (GPH). GPH is the result of the close intraparticle spacing within AuSC and is an important factor in ensuring that NIR-II extinction is achieved. The importance of GPH was demonstrated by early attempts at cluster stabilization and aqueous dispersion through silication, which led to a complete loss of NIR-II LSPR activity due to plasmon damping (Supplementary Fig. 4).[39] From these results, we hypothesized that the tetraethyl orthosilicate monomer was small enough to translocate within the cluster and coat the particles individually. The resulting individual plasmonic peak of AuNPs (~550 nm) was broadened (Supplementary Fig. 4), but the NIR-II peak was entirely absent, since plasmonic coupling would be lost between particles, abrogating GPH.

LSPR spectra of $AuNP_9$ were acquired experimentally, and by simulation using the finite-difference time domain (FDTD) method. The two spectra both possess an LSPR peak at ~550 nm (Fig. 3A, right panel), in agreement with previous literature for AuNPs of this size.[40] The disassembly of AuSC@$(Myrj52)_2$ into $AuNP_9$ abolished all NIR-II LSPR activity, an indicator that persistent intraparticle interaction and GPH are necessary. Large AuNPs (d = 500 nm, $AuNP_{500}$) purchased commercially (Nanopartz, 500-CIT-DIH) were used to determine if AuNPs similar in size to our AuSC@$(Myrj52)_2$ but devoid of GPH would generate a similar LSPR spectrum (Fig. 3B, left and center panels). Experimental and FDTD simulated LSPR spectra displayed a broad LSPR peak at ~600 nm (Fig. 3B, right panel). Both simulated and experimental $AuNP_{500}$ showed a broader and redshifted LSPR peak in comparison to $AuNP_9$. A divergence was observed between the simulated and experimental $AuNP_{500}$ spectra, with experimental spectra showing greater extinction in the NIR-II region than predicted through simulation. Together, the simulated and experimental results for monolithic $AuNP_{500}$ further support the importance of GPH in resulting from persistent intraparticle interactions in AuSCs to produce substantial extinction in the NIR-II region.

To further understand the relationship between the nanomaterial architecture and the spectral properties of the AuSC, we sought to expose the internal structure of AuSC@$(Myrj52)_2$ using Ga focused-ion beam (FIB) milling, followed by helium-ion

microscopy (HIM) of the milled cross-section (Fig. 3C). Upon inspection, our AuSC@$(Myrj52)_2$ appear composed of tightly packed AuNPs, except for a small ~50 nm diameter void, centered within the AuSC (Fig. 3C, center and right panels highlighted by the black arrow). This void was likely generated in the AuNP proclustering step, where AuNPs moving from the oleylamine to *n*-butanol were assembled around residual oleylamine to stabilize the surface energy during solvent transfer. After purification, this immiscible solvent is removed and leaves a central void behind. Intraparticle spacing was impossible to identify as milling artifacts on exposed AuSC faces could not be ruled out. Utilizing the HIM images as guide, simulated extinction spectra were generated by FDTD for several different particle organizations and intraparticle unit cells (IUCs) where the volume between AuNPs within a cluster was varied including non-homogeneous (gradient) spacings, and the observed central void. A complete account of these simulations and their resulting LSPR spectra can be found in Supplementary Fig. 5. Variability in IUCs and organizations generated drastically different extinction spectra. Ultimately, an IUC of 13 nm^3 with a 50 nm diameter central void generated an extinction spectrum similar to that acquired experimentally (Fig. 3D). Simulations of the interaction of broadband light with $AuNP_9$, $AuNP_{500}$, and AuSC@$(Myrj52)_2$ can be seen in Supplementary Videos 1-3, respectively. Both simulated and experimental spectra contained the “bull horn” feature from ~600 nm to ~800 nm, likely a result of the LSPR of the individual AuNPs within the cluster, and the large NIR-II stretch from ~1000 nm to ~1400 nm due to the GPH effect. While $AuNP_{500}$ and AuSC@$(Myrj52)_2$ have a similar diameter, the monolithic $AuNP_{500}$ lack the NIR-II peak feature observed in both simulated and experimental spectra. The absorption and scattering components of these spectra were determined by simulation (Fig. 3E) and experimentally (Fig. 3F). Simulated spectra show the low overall contribution of absorption to the extinction spectra, with a broad peak between ~600 nm to ~800 nm, and a smaller broad peak from ~900 nm to ~1200 nm. The scattering component of the simulated extinction spectra is more dominant across the entire spectral range, with small peaks occurring ~600 nm and ~800 nm relative to the scattering-dominant effects of the AuSC at λ>1000 nm (Fig. 3E). The experimental spectral components deviate from the exact features observed in the simulated spectra, but the overall trend is conserved: absorption is slightly less dominant from 400 nm to 900 nm, but beyond 900 nm the scattering component of the spectra is the primary interaction with light (Fig. 3F).

Differences between the simulated and experimental extinction spectra of AuSC@$(Myrj52)_2$, as well as the absorption and scattering spectra, can be attributed to the fact that FDTD simulations look at a single AuSC, while in a real sample there is a population of AuSC with increased heterogeneity relative to the simulated sample as a result of the material complexity of the assembled AuSC@$(Myrj52)_2$ system. While we have constrained the system to a single IUC value, it is likely that the true IUC values are a gradient between the surface and the core of the cluster. In all AuSC simulations, the original AuNP LSPR peak was accompanied by a secondary absorption maximum in the NIR-II region. This secondary NIR-II maximum was never observed in the simulation of discrete $AuNP_9$ or $AuNP_{500}$. The absorptive behavior of AuSC across

visible wavelengths is unsurprising, given the gray/black visual appearance of AuSC@$(Myrj52)_2$ in solution (Supplementary Fig. 6), but the extensive NIR-II scattering is critical for use as an IV-OCT molecular imaging contrast agent, optimizing the interference effects elicited by AuSCs on the 1350 nm laser light source.

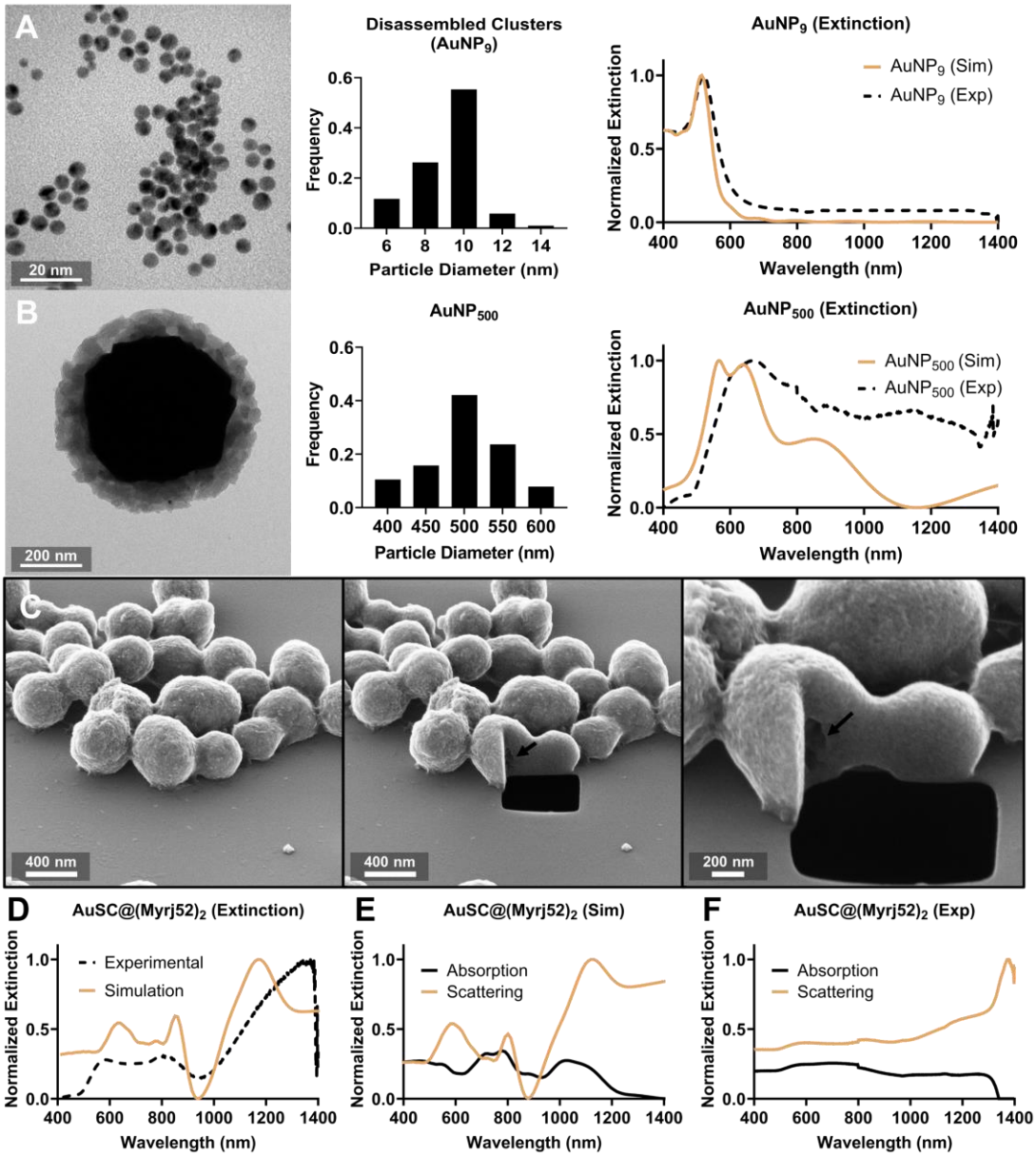

Figure 3. Extinction spectra of AuNPs and AuSC@(Myrj52)$_2$ determined experimentally and by FDTD simulations: A) TEM images of disassembled AuSC@(Myrj52)$_2$ dispersed in hexanes (left panel), their size distribution (n = 105 AuNP$_9$, center panel), as well as experimental and FDTD simulated extinction spectra (right panel). B) TEM (left), size distribution (n = 38 AuNP$_{500}$, centre), and experimental and simulated extinction spectra for d = 500 nm (IQR: 468 – 534 nm) AuNPs (AuNP$_{500}$). Binned histograms in A and B are relative frequencies of particle diameters from TEM. C) HIM images before (left panel) and after (center and right panels) gallium ion beam milling of AuSC@(Myrj52)$_2$. A black arrow highlights the central void. D) Experimental and FDTD simulated AuSC@(Myrj52)$_2$ extinction spectra. E) Simulated absorptive and scattering components of the extinction spectra. F) Absorptive and scattering components of the extinction spectra measured experimentally.

AuSC@(Myrj52)$_2$ enhances IV-OCT imaging contrast:

Image contrast enhancement of dispersions of AuSC@(Myrj52)$_2$, AuNP$_9$, or AuNP$_{500}$ in saline were evaluated in an imaging phantom using a clinical IV-OCT instrument (Abbott Illumien PCT) and clinical imaging catheter (Optis Dragonfly). The phantom and imaging setup are shown in Supplementary Fig. 7. Imaging of a saline solution provided a baseline for IV-OCT contrast (Fig. 4A). AuSC@(Myrj52)$_2$ generated bright, speckled contrast when imaged by IV-OCT over the concentration range 41 µg/mL to 730 µg/mL (Fig. 4A), with contrast enhancement relative to saline of 63.4 ± 0.9 arb. units and 19.3 ± 0.9 arb. Units, respectively (Fig. 4B). The bright signal produced is the result of backscattering of the IV-OCT laser (central wavelength = 1350 nm) by AuSC@(Myrj52)$_2$ (an absorptive effect would lead to a loss of signal).[41] At the same concentration of 365 µg/mL, AuSC@(Myrj52)$_2$ produced substantial image contrast (54.2 ± 2.3 arb. units) compared to AuNP$_9$ (4.7 ± 0.2 arb. units) and AuNP$_{500}$ (18.4 ± 2.7 arb. units). This highlighted the importance of GPH for IV-OCT signal generation, as LSPR and size-mismatched AuNP$_9$ generated almost no contrast enhancement (Fig. 4C). Size-matched AuNP$_{500}$ did generate some IV-OCT contrast due to their weak broad-range scattering,[42] though the similarly sized and plasmon-matched AuSC@(Myrj52)$_2$ improved this signal by nearly 3-fold (Fig. 4C). This result demonstrated the importance of matching the incident light source to a highly scattering spectral component in generating a strong IV-OCT contrast enhancement; though AuNP$_{500}$ and AuSC@(Myrj52)$_2$ are of similar diameter, the strong NIR-II scattering component of AuSC@(Myrj52)$_2$ allows it to generate significantly more IV-OCT contrast than AuNP$_{500}$.

A vascular phantom was generated by filling silicone tubing with an agarose solution doped with either saline, 500 µg/mL AuSC@(Myrj52)$_2$ in saline, or 500 µg/mL AuNP$_9$ in saline, and IV-OCT imaging was performed with a clinical system and imaging catheter (Fig. 4D). Four phantom compositions were created and arranged sequentially in the tubing, then evaluated by a single catheter pullback through the agarose gel. Only the AuSC@(Myrj52)$_2$ showed substantial contrast enhancement relative to agarose containing saline only (Figs. 4D-F). Because of this contrast enhancement, fine structural elements within the phantom (*i.e.*, imperfections in agarose) were more prevalent and detailed when enhanced by AuSC@(Myrj52)$_2$ (Figs. 4E and F). Overall, only AuSC@(Myrj52)$_2$ significantly enhanced IV-OCT contrast relative to background, an outcome of matching the nanomaterial photophysical properties to the laser wavelength of the IV-OCT instrument.

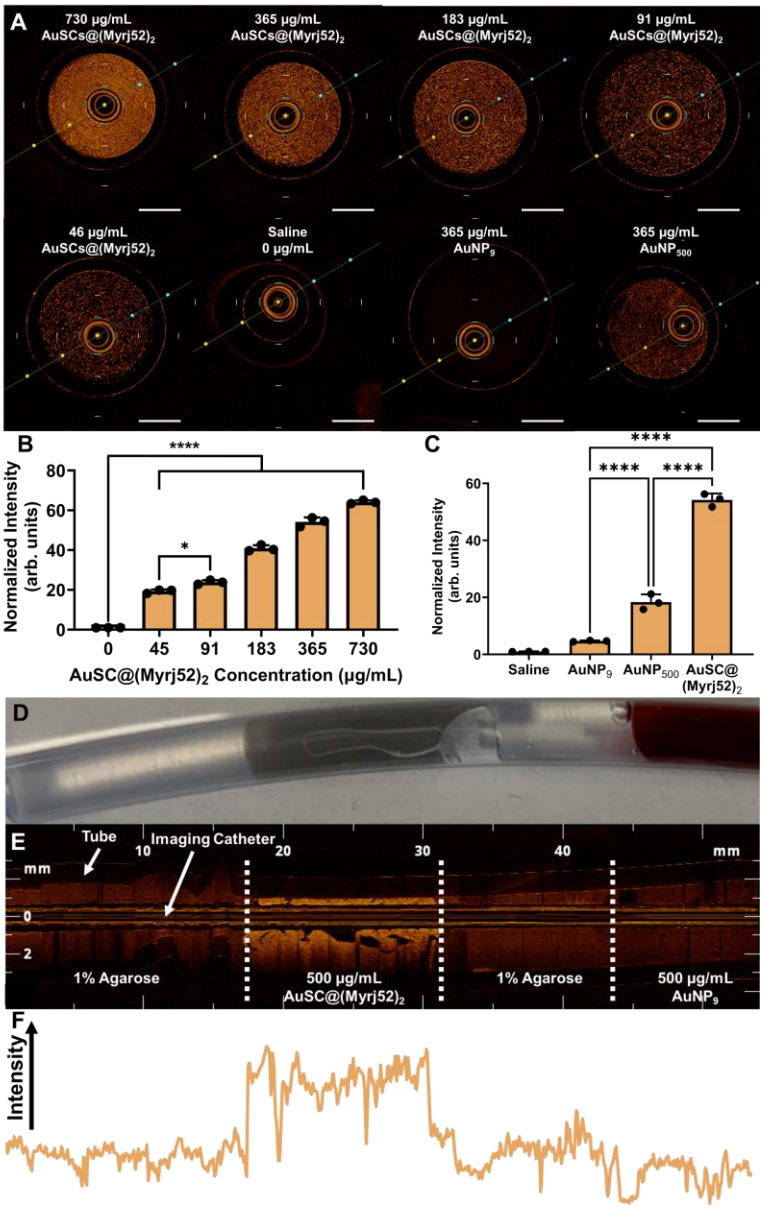

Figure 4. Evaluation of AuSC@(Myrj52)$_2$ performance with an IV-OCT instrument: A) Cross-sections of IV-OCT pullback scans of glass capillaries filled with varying concentrations of AuSC@(Myrj52)$_2$, saline, AuNPs of diameter 9 nm (AuNP$_9$), or AuNPs of diameter 500 nm (AuNP$_{500}$). The white scalebar represents 1 mm. B) Contrast enhancement of AuSC@(Myrj52)$_2$ normalized to saline IV-OCT images. Data are presented as means ± standard deviation for n = 3 cross-sections, *p=0.0103 and ****p<0.0001. C) Contrast enhancement of AuNP$_9$, AuNP$_{500}$, and AuSC@(Myrj52)$_2$ normalized to saline. Data are presented as means ± standard deviation for n = 3 cross-sections, ****p<0.0001. For B) and C), statistical analysis was done by one-way ANOVA followed by a Tukey post hoc test. D) Intravascular phantom composed of a silicone tube filled with agarose doped with saline, AuSC@(Myrj52)$_2$, or AuNP$_9$. E) IV-OCT longitudinal scan of the arterial phantom, aligned to the appropriate regions of the above image in D). F) Signal intensity plot aligned to E) of the IV-OCT pullback of the phantom.

Chemical functionalization AuSC@$(Myrj52)_2$ with a P-selectin targeting mimic facilitates biomolecular recognition:

With the demonstrated superior signal enhancement of AuSC for IV-OCT, we sought to functionalize AuSC@$(Myrj52)_2$ to approach IV-OCT molecular imaging. Our chosen molecular target was P-selectin, a membrane-anchored protein expressed in vascular endothelium as one of the earliest biomolecular responses to inflammation.[43–45] *In vivo,* the cognate ligands of P-selectin include P-selectin glycoprotein ligand-1 (PSGL-1)[46] and sialyl Lewis-X (SLeX)[47,48], which are both expressed on leukocytes as they roll through vasculature to survey for pathology.[49] Neither PSGL1 nor SLeX were suitable as targeting vectors for AuSC due to their complex structures limiting the scale of their production. However, previous reports have shown that the combined display of L-fucose, D-galactose, and an organosulfate group acts as a P-selectin ligand mimic, simulating the sulfated fucose that is imperative for SLeX binding *in vivo*.[50–53]

The functionalization of Myrj52 was achieved through the activation of the terminal primary hydroxyl group using 4-nitrophenolchloroformate (NPC) (Fig. 5A, **2**), resulting in high overall product conversion with the benefit of released NPC acting as a colorimetric indicator of reaction completeness (Fig. 5A). The anomeric carbons of L-fucose and D-galactose were conjugated to HO-$(PEG)_3$-NH_2 groups in the β-anomeric configuration, resulting in a glycoconjugate with nucleophilic handle for polymer conjugation. The resulting functionalized polymers (fuco- (F, Fig. 5A, **2**), galacto- (G, Fig. 5A, **3**), and sulfoMyrj52 (S, Fig. 5A, **4**)) were substituted into the AuSC coating steps, resulting in AuSC@$(xyzFGS)_2$ clusters, where x, y, and z are the molar ratios of each of the F, G, and S functionalized polymers, respectively. Synthetic procedures for the functionalized polymers and a description of all chemical syntheses can be found in the Supplementary Information. All associated nuclear magnetic resonance (NMR) and high-resolution mass spectrometry characterization of these compounds can be found in Supplementary Figs. 8-46.

AuSC@$(xyzFGS)_2$ were evaluated for their P-selectin binding capabilities *in vitro* at 37 °C under agitation, an important factor in the P-selectin-ligand interaction.[54] Ratios of 1:2 F:S, 1:2 G:S, and 1:1:1 F:G:S were assayed for their ability to preferentially bind to P-selectin and bovine serum albumin (BSA) (Fig. 5B, top panel), or BSA-coated wells (Fig. 5B, bottom panel) according to Equation 2. Untargeted AuSC@$(Myrj52)_2$ showed a preferential binding of 70.2 ± 20.4%, while AuSC@$(12FS)_2$, AuSC@$(12GS)_2$, and AuSC@$(111FGS)_2$ showed binding values of 287.7 ± 70.2%, 209.8 ± 22.1%, and 227.6 ± 30.6%, respectively (Fig. 5C). We further evaluated F and S ratios 1:3, 1:1, or 3:1 F:S in this P-selectin ligand mimic on the AuSC surface (Fig. 5D). While at lower AuSC@$(xyFS)_2$ concentrations, the 3:1 formulation significantly outperformed the 1:3 and 1:1 combination, at higher concentrations, the F:S ratio had no significant impact, but consistently increased binding relative to AuSC@$(Myrj52)_2$. Ultimately, AuSC@$(13FS)_2$, was chosen for the *in vivo* studies since higher local concentrations were anticipated at the site of imaging due to direct injection of the contrast agent

through the imaging catheter, as is done clinically. The selection of AuSC@$(13FS)_2$ is also supported by prior literature demonstrating a greater influence of the organosulfate residue on P-selectin binding compared to the carbohydrate residues.[55–57] AuSC LSPR spectra and spherical morphology (Fig. 5E and F, respectively) were unchanged with fucosylation and sulfation. The hydrodynamic size of AuSC@$(13FS)_2$ (Z-average = 514.1 ± 16.5 nm) was significantly greater than AuSC@$(Myrj52)_2$ (Z-average = 431.3 ± 42.6 nm, p = 0.035, Supplementary Fig. 47A). Zeta potential remained unchanged between the two clusters (-37.0 ± 0.9 mV for AuSC@$(Myrj52)_2$ and -37.8 ± 0.4 mV for AuSC@$(13FS)_2$), Supplementary Fig. 47B).

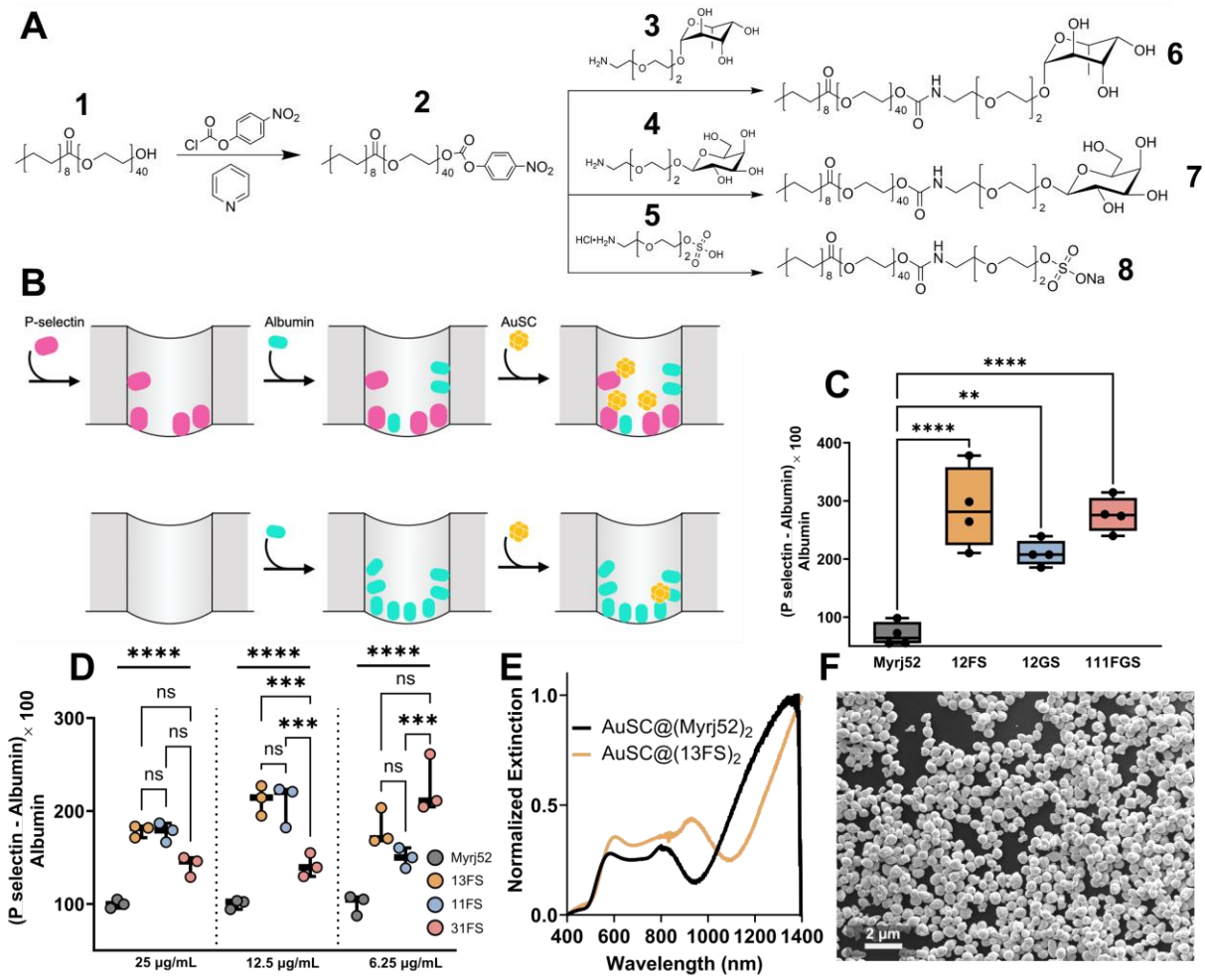

Figure 5. Bioactivation of Myrj52 and evaluation of functionalized AuSC binding to P-selectin *in vitro*. A) Synthetic overview of Myrj52 activation and functionalization. B) Illustration of the P-selectin binding assay. C) Comparison of 25 µg/mL Au AuSC@(Myrj52)$_2$ (gray), 12FS (orange), 12GS (blue), or 111FGS (pink) preferential binding to P-selectin *in vitro*. Data presented are boxplots of n = 3 replicate binding assays. Statistical analysis was done by one-way ANOVA followed by a Tukey post-hoc test. ****p<0.0001, **p=0.002. D) *In vitro* evaluation of different concentrations (25, 12.5, and 6.25 µg/mL of Au) of AuSC@(Myrj52)$_2$ (gray), 13FS (orange), 11FS (blue), and 31FS (pink). Data presented are boxplots of n = 3 replicate binding assays, normalized to the Myrj52 binding value. Statistical analysis was done by two-way ANOVA followed by a Tukey post-hoc test. ****p<0.0001, ***p<0.001. E) Extinction spectra of AuSC@(Myrj52)$_2$ and AuSC@(13FS)$_2$ in water. F) SEM image of AuSC@(13FS)$_2$.

Molecular IV-OCT enabled by AuSC@$(13FS)_2$ to map early intravascular inflammation *in vivo*:

In routine stent evaluation by IV-OCT, common radial artifacts due to the stent arise, known as bloom (the result of laser backscattering) and merry-go-round (the result of laser attenuation or shadowing).[58,59] The binding of AuSC@$(13FS)_2$ to endovascular P-selectin would result in the accumulation of metal at the endovascular surface and the generation of both bloom and merry-go-round image features, which we termed as Reflection or scattering events (ROSEs) (Fig. 6A). Intravascular inflammation in rats was induced through the administration of LPS *i.v.*, which was previously reported to stimulate intravascular P-selectin expression in rodents.[60–62] Dosage and incubation times that led to maximal P-selectin expression in rats were determined and validated experimentally, with 4 mg/kg LPS and 4 hr resulting in extensive P-selectin expression (Supplementary Fig. 48). IV-OCT using a clinical instrument (Abbott Illumien PCT) and clinical imaging catheter (Optis Dragonfly) was performed on rats injected with LPS or saline (naïve) following the dissection and clamping of their abdominal aorta (AA), and insertion of the imaging catheter. Rats remained alive during this procedure. The AA was chosen as it was the only vasculature large enough to accommodate the 2 mm diameter imaging catheter. Saline was flushed *via* the imaging catheter port until blood was removed, as is performed clinically, and a baseline image was acquired while under 4 mL/min saline flow to maintain vascular patency (Fig. 6B, top panel). The AA was flushed with AuSC@$(13FS)_2$ or AuSC@$(Myrj52)_2$ through the imaging catheter, incubated for 30 s, then flushed with saline to clear unbound clusters prior to image acquisition (Fig. 6B, bottom panel). LPS-treated rats showed little to no ROSEs before and after flushing with AuSC@$(Myrj52)_2$ (Fig. 6B, left panels), while AuSC@$(13FS)_2$ showed numerous ROSEs that were not present prior to contrast flush (Fig. 6B, center panels). Naïve rats showed no ROSEs before or after AuSC@$(13FS)_2$ flush. (Fig. 6C, right panels). A video of the full vessel length imaged can be seen in Supplementary Video 4.

Quantitative analysis of AuSC binding was performed in a blinded evaluation of the number of ROSEs observed *per* cm length of artery imaged (Fig. 6C). Significantly more ROSEs were generated in LPS-treated rats (Fig. 6C) with AuSC@$(13FS)_2$ (11.2 ± 8.9 ROSEs/cm) compared to AuSC@$(Myrj52)_2$ (1.9 ± 1.5 ROSEs/cm). Some binding in healthy tissue was expected as the plate-binding assay did show some non-specific adhesion of AuSC@$(Myrj52)_2$. A significant reduction in AuSC@$(13FS)_2$ induced ROSE generation was observed in healthy rats (0.2 ± 0.4 ROSEs/cm), which supported the specificity of the AuSC@$(13FS)_2$-P-selectin interaction. The high standard deviation of AuSC@$(13FS)_2$ ROSEs was due to the variability in inflammation severity in the rat LPS model (Supplementary Fig. 49). Blindly scored histological sections of the AA stained with anti-CD62p (anti-P-selectin antibody) showed a linear correlation between P-selectin expression (inflammation severity) and contrast agent binding (ROSEs/cm), suggesting that AuSC@$(13FS)_2$ molecular imaging can indicate arterial disease severity (Fig. 6D, $R^2 = 0.751$, $p < 0.05$). Superclusters were stable even after overnight

incubation in mouse serum as indicated by the maintenance of the NIR-II LSPR peak and presence of AuSC by SEM (Supplementary Fig. 50). Therefore, AuSC would still generate strong scattering signal even in the presence of remaining sera factors, though these are routinely flushed prior to IV-OCT clinical imaging. These results support the utility of AuSC@$(13FS)_2$ as an IV-OCT molecular imaging agent for vascular inflammation, and broadly support the application of AuSC as a molecular imaging platform capable of adding molecular-level information to IV-OCT without changing the current clinical workflow.

AuSC@$(13FS)_2$ biodistribution was quantified by ICP-MS analysis (Supplementary Fig. 51) following *i.v.* injection at a dose that was ~5× more concentrated than that used for imaging. All injections were well-tolerated by the animals, with no symptoms of toxic response. Significant Au deposition was only observed in the spleen, which appeared to be the primary route of AuSC@$(13FS)_2$ clearance. This is a common route of blood clearance for nanoparticles of this size.[63,64] Given the low %ID/g wet tissue observed at the earliest timepoint of 1 hr post-injection, it is likely AuSC@$(13FS)_2$ clears rapidly. Histological evaluation of tissues involved in blood clearance showed no change in morphology up to 24 hr post-injection (Supplementary Fig. 52).

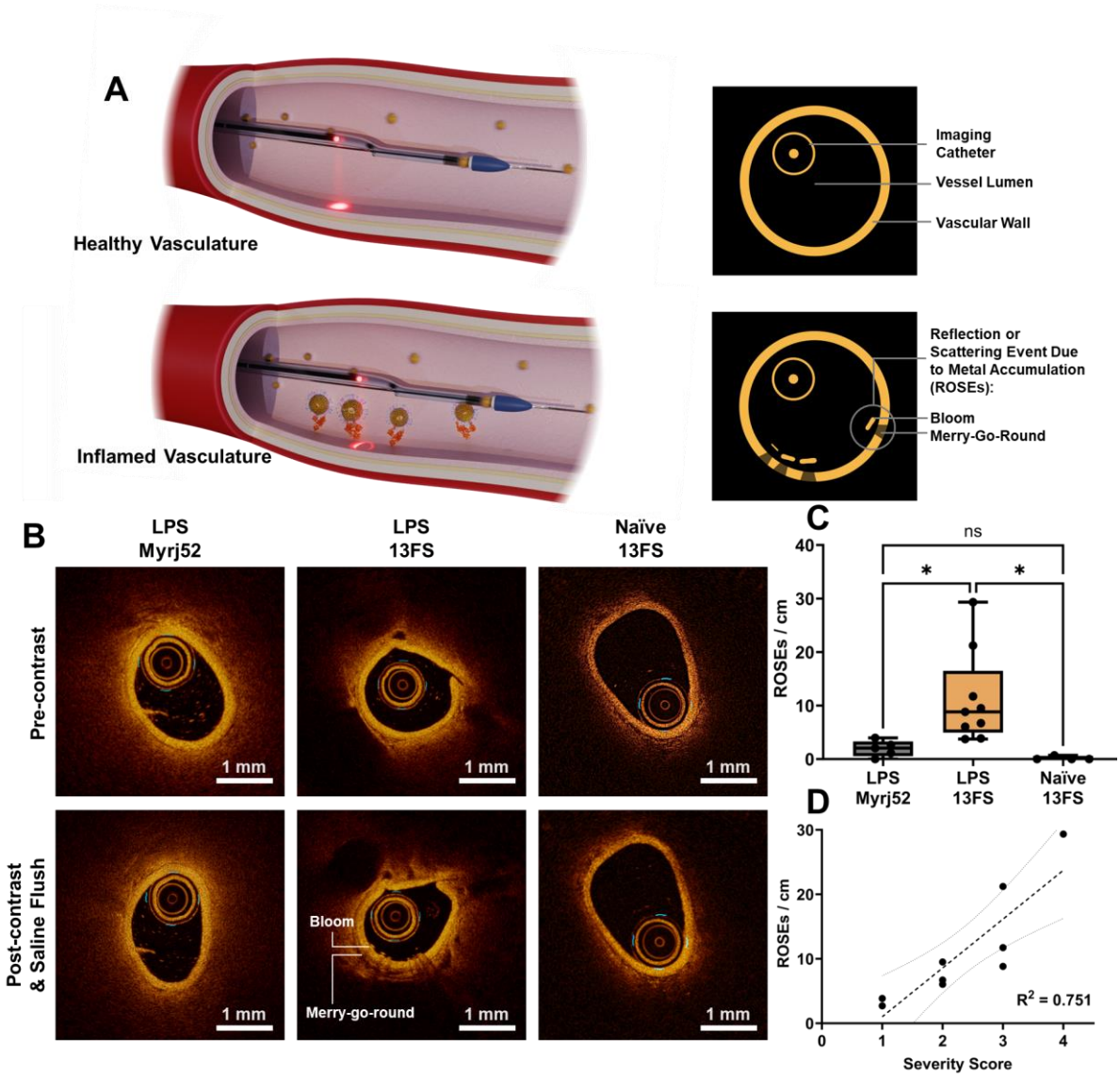

Figure 6. *In vivo* IV-OCT molecular imaging of intravascular inflammation with AuSC@(13FS)$_2$. A) Illustration of the expected binding interactions of AuSC@(13FS)$_2$ in healthy (top) and inflamed (bottom) arteries, and the hypothesized tomographs with AuSC binding-associated reflection or scattering events (ROSEs). B) Two-dimensional IV-OCT cross sections of rat abdominal aorta (AA) before (top panel) and after (bottom panel) AuSC@(Myrj52)$_2$ or AuSC@(13FS)$_2$ flush, following a saline flush in inflamed (left and centre) and healthy (right) rats. C) ROSEs generated per centimeter in the rat abdominal aorta (AA). Data are presented as boxplots of n = 5 (LPS, Myrj52), n = 9 (LPS, 13FS), and n = 4 (naïve, 13FS) rats. *p<0.05. Statistical analysis was done by one-way ANOVA followed by a Tukey post-hoc test. D) Correlation between histological severity score of anti-CD62p rat AAs correlated to their ROSEs/cm for AuSC@(13FS)$_2$ in LPS-treated rats. The dotted line represents a linear fit with R^2 = 0.751. Dashed lines above and below represent the error bands.

Conclusions:

Herein we have shown a facile, rapid, and scalable synthetic approach for the one-pot generation and controlled superclustering of oleylamine capped AuNPs. The concept of solvophobically-driven superclustering demonstrated here with $HAuCl_4$ will likely parallel that with using other capping agents and other plasmonic nanoparticles, due to the dependence on solvent-driven assembly. We have also demonstrated the importance of persistent particle stabilization in generating a large redshift through GPH, as well as how changes in IUCs can be used to tailor the LSPR response. Polymer-mediated AuSC stabilization facilitates aqueous dispersion of the clusters without changing their optical properties. Ultimately, solvent and stabilizer can be used in concert to tailor IUC and tune the LSPR of the resulting superclusters.

Towards introducing IV-OCT molecular imaging, we have synthesized three novel polymers bearing fucosyl, galactoyl, and sulfyl functional groups that, in combination, form a P-selectin ligand on our AuSC. The ligand combination resulted in binding to P-selectin both *in vitro* and *in vivo*. The absence of change to the physicochemical properties of AuSC due to the introduction of the target ligand indicates a high degree of physicochemical compatibility for terminal functionalization of Myrj52, allowing these NIR-II scattering superclusters to serve as a platform for molecular imaging in IV-OCT. Finally, we have demonstrated the first instance of *in vivo* molecular imaging with IV-OCT using our AuSC@$(13FS)_2$ contrast agent in live rats with LPS-stimulated P-selectin expression. Given the modularity of the surface functionalization and the tolerability of conjugation strategies to many functional groups and polymers, further efforts to improve on binding, or target different biomolecules of inflammation can create a more personalized approach to diagnostics in IV-OCT without sacrificing the core technology of generating ROSEs by target engagement. AuSC@$(13FS)_2$ target binding and immobilization generates ROSE artifacts like those seen due to placed stents and stand out in comparison to other IV-OCT image features, allowing the easy identification of regions of endovascular inflammation. Overall, we have demonstrated that these highly NIR-II scattering, P-selectin targeting AuSC@$(13FS)_2$ may serve as the genesis of more personalized cardiovascular medicine through IV-OCT molecular imaging.

Methods:

All animal studies were conducted under Animal Use Protocol HIe-3652 approved by the IACUC at the University of Ottawa. Rats were housed doubly under a 12 h light/dark cycle, and ambient temperature of 20-24°C and 45 to 65% humidity. All rats were provided access to food (Rodent Laboratory Chow) and water *ad libitum*.

General Reagents:

All chemical reagents were purchased from Sigma-Aldrich and used as is unless otherwise reported, apart from mouse P-selectin which was purchased from Sino Biologics Inc. (50737-M08H). All solvents were HPLC grade, except for water (18.2 MΩ cm Millipore water).

Experimental Procedures:

All AuSC reaction mixtures were degassed and backflushed with N_2 prior to microwave-assisted synthesis on a CEM Discovery SP microwave. For all AuSC syntheses, power was set to 75 W and the reaction was held for 90 s at 115°C. All AuSC and AuNP concentrations are reported as µg/mL as determined by ICP-OES on an Agilent 700 after 4 hr solubilization at 80°C by aqua regia (3:1 HCl:HNO_3) and dilution in water. LSPR spectra were acquired using a Cary 7000 UV-Vis-NIR spectrometer. All spectra were presented normalized from 0 to 1, with 0 being the lowest signal and 1 being the highest to adequately compare spectra with concentration dissimilarities, as well as to compare between experimental and simulated spectra. All TEM images were acquired using an FEI Tecnai G2 Spirit Twin TEM, all SEM images were acquired using a JEOL JSM-7500F field emission SEM, all HIM images were acquired using a NAME. All IV-OCT imaging was performed using an Abbott Illumien™ OPTIS™ PCI instrument using Dragonfly™ OPTIS™ imaging catheters and 54 mm high-resolution pullback imaging. All image analyses and quantifications were performed using FIJI. GraphPad Prism 10.0 was used to generate all graphs, graphical figures, and statistical analyses.

General method for AuSC@(Myrj52)$_2$ and AuSC@(xyzFGS)$_2$ synthesis:

In a typical synthesis, $HAuCl_4 \cdot 3H_2O$ (40 mg, 0.1 mmol) was dissolved in ethylene glycol (2 mL) in a three-neck round bottom flask under stirring at 45°C. Oleylamine (70%, 4 mL) and ethylene glycol (4 mL) were added to the flask and the entire solution was degassed until effervescence ceased (~45 min). The flask was backflushed with N_2 and the contents decanted into an N_2-purged 35 mL microwave reaction vial. The vial was capped with a Teflon cap and inserted into a CEM Discovery SP microwave reactor, where the solution was heated at 75 W (~0.65°C / s), with reaction held at 115°C for 90 s, at which point the solution was cooled by blowing air onto the vessel, which was released from the reactor at 50°C. These stabilized AuSC were immediately added to a 40 mL solution of n-butanol containing functionalized or unfunctionalized Myrj52 (20 g/L) and was agitated overnight. The solution was centrifuged at room temperature (RT, 1000 xg, 10 min), decanted, replenished with

fresh n-butanol (40 mL) not containing polymers, and sonicated back into dispersion. Centrifugation washes were repeated three times, with the mono-coated AuSC pellet after the third centrifugation being re-dispersed by sonication in an aqueous (water or saline) solution of functionalized or unfunctionalized Myrj52 (40 mL, 40 g/L). AuSC in aqueous polymeric solution were shaken overnight, followed by centrifugation (RT, 1000 xg, 10 min), decanting, and re-dispersion by sonication into fresh aqueous solution (40 mL) not containing the polymers. Centrifugation washes were repeated three times, with the pellet being resuspended in 2 mL of aqueous solvent after the final centrifugation. The doubly-coated AuSC concentrate was twice-purified by size exclusion column chromatography (Pd10 column) eluting with water. Resulting AuSC were allowed to settle overnight, were decanted, and resuspended in 1 – 2 mL of fresh aqueous solution without polymers. Aqueously dispersed AuSC were stored at 4^{o}C. AuSC concentration (μg/mL Au) was determined by ICP-OES analysis of an aliquot of this solution.

AuSC and AuNP size measurements by TEM image analysis:

AuNPs or AuSC (stabilized, mono-, or di-coated) were drop cast and dried on the carbon-coated side of Cu TEM grid with mesh size 300 and dried overnight. Acquired TEM images were loaded into FIJI and turned into binary images. A watershed function was applied, and the “analyze particles” function was used to automatically measure the area of clusters or particles within the field of view. The resulting area was used to solve for diameter of the AuNPs or AuSC. Sizes were presented as a relative frequency distribution of binned diameters, with the relative frequency describing the amount of occurrence of one bin value. The same grids used for TEM imaging were also used for subsequent SEM imaging.

AuSC and AuNP LSPR spectra acquisition:

AuNPs or AuSC (stabilized, mono-, or di-coated) were dispersed in their appropriate solvent and placed in a low-volume (700 μL) black-walled cuvette. All extinction spectra were zeroed and blanked by the plain dispersion solvent at 0% and 100% transmission prior to extinction spectra acquisition of samples.

The Cary 7000 UV-Vis-NIR was equipped with an external DRA-2500 attachment; a large integrating sphere that allowed for the separation of scattering and absorptive components of the extinction spectra by collection of the scattered component. We used 1.5 cm glass-walled cuvettes compatible with NIR-II light in a center-mount cuvette holder made for the external DRA-2500 (Agilent). Scattering spectra was zeroed and blanked by water at 0% and 100% transmission prior to acquisition of scattering spectra. The resulting scattering spectra was subtracted from the previously acquired extinction spectra to generate the absorption spectra.

Milling and HIM imaging of AuSC@(Myrj52)$_2$:

A TEM grid drop-casted with AuSC@(Myrj52)$_2$ as previously described was used for all milling and HIM imaging. Grids were loaded into a Zeiss Orion NanoFAB with Ga

FIB. Clusters were quartered with the Ga FIB (10 pA, 25 µm aperture, 30 kV landing energy, dwell time 0.1 µs, and 0.15 nC/µm^2 dose). HIM images before and after milling were acquired using a gas-field ion source with different fields of view. Low magnification HIMs were acquired with a beam current of 1.53 pA and a dwell time of 1 µs, while high magnification images were acquired with a beam current of 1.08 pA and a dwell time of 0.5 µs.

FDTD modelling and spectra simulation:

The simulated results were obtained through an in-house finite-difference time-domain (FDTD) electrodynamic solver that is parallelized for high performance computing.[65] The solver is deployed on the Digital Research Alliance of Canada High Performance Computing network, using up to a maximum of 800 cores, and running continuously for over 24 hr. The simulation domain consists of uniform ($\Delta x = \Delta y = \Delta z$) Yee cells with a side length of 0.5 nm that is excited by a plane-wave broadband raised cosine source (Equation 1),

$$s(t) = \frac{1}{8}(1 - \cos \omega_{max} t)^3 \quad \textbf{Eq. 1}$$

where $\omega_{max} = 2\ \mathrm{PHz}$. The simulation domain size for the AuSC is 620 nm (1240 cells) in each direction, terminated by 20 convolutional perfectly matched layer cells on each face of the cubic domain. The extinction spectrum is obtained through the scattering and absorption cross sections that are measured via the “Poynting vector flux method”.[65]

The superclusters whose results are shown in Fig 3 D-F are modelled as a spherical shell composed of 9 nm diameter gold spheres, arranged in a face-centered cubic (FCC) lattice with an outer radius of 209 nm and an inner radius of 50 nm, and centre-to-centre interparticle spacing of 13 nm. This lattice is embedded into a sphere of the amphiphilic polymer of the same diameter. The superclusters are located within a background material of water. The dispersive behaviour of gold is modelled by a Drude model with two critical points, implemented using the auxiliary differential equation technique.[66] Water and amphiphilic polymers were modelled as non-dispersive media with fixed refractive indices of n = 1.33 and n = 1.46 respectively.

in vitro IV-OCT imaging of AuSC@(Myrj52)$_2$:

Cross-sectional imaging:

To prevent external light interference, imaging was performed inside of a Styrofoam box, which was pierced by a glass Pasteur pipette containing an AuSC suspension. The imaging catheter was inserted into the thin end of the pipette external to the box and the portion of the pipette inside of the box was imaged by pullback. A picture of this setup can be seen in Supplementary Fig. 7. The integrated density of a consistent area and region of the cross-sections generated by the longitudinal imaging was acquired using FIJI and normalized to the weakest contrast enhancer, AuNP$_9$.

Vascular phantom and longitudinal imaging:

A 2% agarose solution was prepared by heating 50 mL of water containing 500 mg of agarose. The hot solution was mixed 1:1 with 1 mg/mL AuSC@$(Myrj52)_2$, 1 mg/mL $AuNP_9$, or water. These solutions were serially injected into a piece of silicone tubing cooled at 4°C for 2 hr. The tube was placed in the same Styrofoam box setup, pierced by a glass pipette, and catheterized within the box. IV-OCT pullback imaging was performed to generate a longitudinal image of the phantom. The integrated density across the bottom portion of the longitudinal image was normalized from 0 (lowest integrated density value) to 1 (highest integrated density value) to generate the intensity curve associated with the image.

in vitro P-selectin binding assay:

Highly hydrophobic 96-well plates were incubated with 50 µl of 1X Tris-buffered saline solution containing 1 mM $CaCl_2$ (pH 7.4, TBS) alone or with mouse recombinant P-selectin (2 µg/mL) overnight at 4°C. The wells were washed three times with TBS, and then incubated overnight at 4°C with 150 µl of bovine serum albumin (BSA, 3%) in TBS to block non-coated areas of the wells. The wells were washed three times with 1 mM $CaCl_2$ in Milli-Q water, then incubated with different concentrations or different ratios of AuSC$(xyzFGS)_2$ in Milli-Q water with 1 mM $CaCl_2$ at 37°C on a plate shaker at 700 RPM for 15 min. The wells were washed three times with Milli-Q water to remove unbound clusters. Aqua regia (200 µl) was added to each well and the plate was left at room-temperature over the weekend to digest the remaining clusters. The digest solution was diluted with Milli-Q water and Au concentration was determined by ICP-MS. Preferential binding was expressed as a normalized ratio of the concentration of AuSC@$(xyzFGS)_2$ bound to P-selectin-coated wells compared to BSA-coated wells according to Equation 2:

$$\frac{[BoundAuSC]_{Psel} - [BoundAuSC]_{BSA}}{[BoundAuSC]_{BSA}} \qquad \textbf{Eq. 2}$$

Targeting P-selectin in rat in vivo *model:*

Sprague-Dawley rats (12 weeks old, Charles River) were injected *iv* with LPS (*Escherichia coli* O111:B4, 4 mg/kg in saline) or saline, which was allowed to circulate for 4 hr. Rats were anesthetized with isoflurane and dissected to expose the AA. The AA was clamped, severed, and catheterized with the IV-OCT imaging catheter. A syringe pump connected to the injection port of the imaging catheter pumped saline through the AA at 3.5 mL/min. Once clear of blood, a 54 mm high-resolution pullback image was acquired. Flow was interrupted and 100 µl of 500 µg/mL AuSC@$(13FS)_2$ was injected through the imaging catheter and allowed to incubate in the AA for 30 s. Flow of saline at 3.5 mL/min was resumed, and once excess cluster was flushed out another pullback image was acquired. The catheter was removed, and rats were euthanized by exsanguination. The section of catheterized AA was removed and left in 10% formalin in

phosphate-buffered saline (pH 7.4) overnight, then replaced by 70% ethanol the next day. Tissue was mounted in paraffin, sliced, and stained with anti-CD62p to evaluate P-selectin expression within the AA. These sections were scored by a blinded participant.

DICOMs of IV-OCT pullbacks were cropped to include usable images of the AA (minimum 3 cm of AA length). Each slice (0.01 cm) was evaluated to determine if a ROSE was visible. A ROSE must have both the bloom and merry-go-round features to be included as a count.

Statistical analyses:

Statistical analyses were performed using GraphPad Prism 10.0 (GraphPad, Inc.). Comparisons across more than two groups was performed by one-way ANOVA followed by Tukey's test for honestly significant differences. Normality was assumed where appropriate for all data sets. Prior to ANOVA, Levene's test was used to confirm equal variance, and visual quantile-quantile plot analysis was used to confirm homoscedasticity.

Data Availability:

All raw and source data is available on request of the corresponding author.

Code Availability:

Code is available upon reasonable request from Dr. Lora Ramunno.

References:

1. Feng, Z. *et al.* Perfecting and extending the near-infrared imaging window. *Light: Science & Applications 2021 10:1* **10**, 1–18 (2021).
2. Cao, J. *et al.* Recent Progress in NIR-II Contrast Agent for Biological Imaging. *Front Bioeng Biotechnol* **7**, 1–21 (2020).
3. Zhang, N. nan *et al.* Recent advances in near-infrared II imaging technology for biological detection. *J Nanobiotechnology* **19**, 1–14 (2021).
4. Xu, H. *et al.* NIR-II-absorbing diimmonium polymer agent achieves excellent photothermal therapy with induction of tumor immunogenic cell death. *J Nanobiotechnology* **21**, 132 (2023).
5. Yang, Q., Ma, H., Liang, Y. & Dai, H. Rational Design of High Brightness NIR-II Organic Dyes with S-D-A-D-S Structure. *Acc Mater Res* **2**, 170–183 (2021).
6. Li, Z. *et al.* NIR-II Functional Materials for Photoacoustic Theranostics. *Bioconjug Chem* **33**, 67–86 (2022).
7. Su, Y., Yu, B., Wang, S., Cong, H. & Shen, Y. NIR-II bioimaging of small organic molecule. *Biomaterials* **271**, 120717 (2021).
8. Sun, X. *et al.* Effects of nanoparticle sizes, shapes, and permittivity on plasmonic imaging. *Optics Express, Vol. 30, Issue 4, pp. 6051-6060* **30**, 6051–6060 (2022).
9. Zhuang, Y. *et al.* Size and Shape Effect of Gold Nanoparticles in “Far-Field” Surface Plasmon Resonance. *Particle & Particle Systems Characterization* **36**, 1800077 (2019).
10. González, A. L., Noguez, C., Beránek, J. & Barnard, A. S. Size, shape, stability, and color of plasmonic silver nanoparticles. *Journal of Physical Chemistry C* **118**, 9128–9136 (2014).
11. Bezerra, H. G., Costa, M. A., Guagliumi, G., Rollins, A. M. & Simon, D. I. Intracoronary Optical Coherence Tomography: A Comprehensive Review: Clinical and Research Applications. *JACC Cardiovasc Interv* **2**, 1035–1046 (2009).
12. Roleder, T. *et al.* The basics of intravascular optical coherence tomography. *Postepy Kardiol Interwencyjnej* **11**, 74 (2015).
13. Gounis, M. J. *et al.* Intravascular Optical Coherence Tomography for Neurointerventional Surgery. *Stroke* **50**, 218–223 (2019).
14. Megaly, M. *et al.* Radial Versus Femoral Access in Chronic Total Occlusion Percutaneous Coronary Intervention: A Systematic Review and Meta-Analysis. *Circ Cardiovasc Interv* **12**, (2019).
15. Swanson, E. A. & Fujimoto, J. G. The ecosystem that powered the translation of OCT from fundamental research to clinical and commercial impact [Invited]. *Biomed Opt Express* **8**, 1638 (2017).

16. McCabe, J. M. & Croce, K. J. Optical coherence tomography. *Circulation* **126**, 2140–2143 (2012).

17. Yonetsu, T. *et al.* Plaque morphologies and the clinical prognosis of acute coronary syndrome caused by lesions with intact fibrous cap diagnosed by optical coherence tomography. *Int J Cardiol* **203**, 766–774 (2016).

18. Toutouzas, K., Karanasos, A. & Tousoulis, D. Optical Coherence Tomography For the Detection of the Vulnerable Plaque. *European Cardiology Review* **11**, 90 (2016).

19. Wang, A., Qi, W., Gao, T. & Tang, X. Molecular Contrast Optical Coherence Tomography and Its Applications in Medicine. *Int J Mol Sci* **23**, 3038 (2022).

20. Ameh, T. *et al.* Silver and Copper Nanoparticles Induce Oxidative Stress in Bacteria and Mammalian Cells. *Nanomaterials* **12**, (2022).

21. Mondal, I., Raj, S., Roy, P. & Poddar, R. Silver nanoparticles (AgNPs) as a contrast agent for imaging of animal tissue using swept-source optical coherence tomography (SSOCT). *Laser Phys* **28**, (2018).

22. Marin, R. *et al.* Plasmonic Copper Sulfide Nanoparticles Enable Dark Contrast in Optical Coherence Tomography. *Adv Healthc Mater* **9**, 1901627 (2020).

23. Cabuzu, D., Cirja, A., Puiu, R. & Grumezescu, A. Biomedical applications of gold nanoparticles. *Curr Top Med Chem* **15**, 1605–1613 (2015).

24. Si, P. *et al.* Gold nanomaterials for optical biosensing and bioimaging. *Nanoscale Adv* **3**, 2679–2698 (2021).

25. Si, P. *et al.* Gold Nanoprisms as Optical Coherence Tomography Contrast Agents in the Second Near-Infrared Window for Enhanced Angiography in Live Animals. *ACS Nano* **12**, (2018).

26. Nguyen, V. P. *et al.* Gold Nanorod Enhanced Photoacoustic Microscopy and Optical Coherence Tomography of Choroidal Neovascularization. *ACS Appl Mater Interfaces* **13**, (2021).

27. Zhao, Y. *et al.* A comparison between sphere and rod nanoparticles regarding their in vivo biological behavior and pharmacokinetics. *Sci Rep* **7**, 4131 (2017).

28. Hu, J. *et al.* Gold nanoshells: Contrast agents for cell imaging by cardiovascular optical coherence tomography. *Nano Res* **11**, 676–685 (2018).

29. Hu, J. *et al.* Optical Nanoparticles for Cardiovascular Imaging. *Adv Opt Mater* **6**, 1800626 (2018).

30. Muñoz-Ortiz, T. *et al.* Molecular Imaging of Infarcted Heart by Biofunctionalized Gold Nanoshells. *Adv Healthc Mater* **10**, 2002186 (2021).

31. Hu, J. *et al.* Dynamic single gold nanoparticle visualization by clinical intracoronary optical coherence tomography. *J Biophotonics* **10**, 674–682 (2017).

32. Kwon, N. *et al.* Direct Chemical Synthesis of Plasmonic Black Colloidal Gold Superparticles with Broadband Absorption Properties. *Nano Lett* **18**, 5927–5932 (2018).

33. Yu, J. H. *et al.* Highly Excretable Gold Supraclusters for Translatable In Vivo Raman Imaging of Tumors. *ACS Nano* **17**, (2023).

34. Gulumian, M., Andraos, C., Afantitis, A., Puzyn, T. & Coville, N. J. Importance of Surface Topography in Both Biological Activity and Catalysis of Nanomaterials: Can Catalysis by Design Guide Safe by Design? *International Journal of Molecular Sciences 2021, Vol. 22, Page 8347* **22**, 8347 (2021).

35. Witika, B. A. *et al.* Biocompatibility of Biomaterials for Nanoencapsulation: Current Approaches. *Nanomaterials 2020, Vol. 10, Page 1649* **10**, 1649 (2020).

36. Ethylene glycol monostearate | C20H40O3 | CID 24762 - PubChem. https://pubchem.ncbi.nlm.nih.gov/compound/Ethylene-glycol-monostearate#section=Interactions.

37. Rahmani, M. *et al.* Beyond the hybridization effects in plasmonic nanoclusters: Diffraction-induced enhanced absorption and scattering. *Small* **10**, 576–583 (2014).

38. Nordlander, P., Oubre, C., Prodan, E., Li, K. & Stockman, M. I. Plasmon hybridization in nanoparticle dimers. *Nano Lett* **4**, 899–903 (2004).

39. Lee, S. A. & Link, S. Chemical Interface Damping of Surface Plasmon Resonances. *Acc Chem Res* **54**, 1950–1960 (2021).

40. Polavarapu, L., Venkatram, N., Ji, W. & Xu, Q. H. Optical-limiting properties of oleylamine-capped gold nanoparticles for both femtosecond and nanosecond laser pulses. *ACS Appl Mater Interfaces* **1**, 2298–2303 (2009).

41. Aumann, S., Donner, S., Fischer, J. & Müller, F. Optical Coherence Tomography (OCT): Principle and Technical Realization. *High Resolution Imaging in Microscopy and Ophthalmology* 59–85 (2019) doi:10.1007/978-3-030-16638-0_3.

42. Huang, X. & El-Sayed, M. A. Gold nanoparticles: Optical properties and implementations in cancer diagnosis and photothermal therapy. *J Adv Res* **1**, 13–28 (2010).

43. Burger, P. C. Platelet P-selectin facilitates atherosclerotic lesion development. *Blood* **101**, 2661–2666 (2003).

44. Lorenzon, P. *et al.* Endothelial Cell E- and P-Selectin and Vascular Cell Adhesion Molecule-1 Function as Signaling Receptors. *J Cell Biol* **142**, 1381–1391 (1998).

45. Harari, O. A. *et al.* Endothelial cell E- and P-selectin up-regulation in murine contact sensitivity is prolonged by distinct mechanisms occurring in sequence. *J Immunol* **163**, 6860–6 (1999).

46. Moore, K. L. Structure and Function of P-Selectin Glycoprotein Ligand-1. *Leuk Lymphoma* **29**, 1–15 (1998).

47. Beauharnois, M. E. *et al.* Affinity and kinetics of sialyl lewis-X and Core-2 based oligosaccharides binding to L- and P-selectin. *Biochemistry* **44**, 9507–9519 (2005).

48. Zandberg, W. F., Kumarasamy, J., Pinto, B. M. & Vocadlo, D. J. Metabolic Inhibition of Sialyl-Lewis X Biosynthesis by 5-Thiofucose Remodels the Cell Surface and Impairs Selectin-Mediated Cell Adhesion. *J Biol Chem* **287**, 40021 (2012).

49. Beste, M. T. & Hammer, D. A. Selectin catch-slip kinetics encode shear threshold adhesive behavior of rolling leukocytes. *Proc Natl Acad Sci U S A* **105**, 20716–20721 (2008).

50. Pudelko, M., Bull, J. & Kunz, H. Chemical and Chemoenzymatic Synthesis of Glycopeptide Selectin Ligands Containing Sialyl Lewis X Structures. *ChemBioChem* **11**, 904–930 (2010).

51. Revelle, B. M., Scott, D., Kogan, T. P., Zheng, J. & Beck, P. J. Structure-function analysis of P-selectin-sialyl LewisX binding interactions. Mutagenic alteration of ligand binding specificity. *J Biol Chem* **271**, 4289–4297 (1996).

52. Galustian, C. *et al.* Synergistic interactions of the two classes of ligand, sialyl-Lewisa/x fuco-oligosaccharides and short sulpho-motifs, with the P- and L-selectins: implications for therapeutic inhibitor designs. *Immunology* **105**, 350 (2002).

53. Rodgers, S. D., Camphausen, R. T. & Hammer, D. A. Sialyl Lewis(x)-mediated, PSGL-1-independent rolling adhesion on P-selectin. *Biophys J* **79**, 694 (2000).

54. Rutledge, N. S. & Muller, W. A. Understanding Molecules that Mediate Leukocyte Extravasation. *Curr Pathobiol Rep* **8**, 25–35 (2020).

55. Manning, D. D., Hu, X., Beck, P. & Kiessling, L. L. Synthesis of sulfated neoglycopolymers: Selective P-selectin inhibitors. *J Am Chem Soc* **119**, 3161–3162 (1997).

56. Dernedde, J. *et al.* Dendritic polyglycerol sulfates as multivalent inhibitors of inflammation. *Proc Natl Acad Sci U S A* **107**, 19679–19684 (2010).

57. John, A. E. *et al.* Discovery of a potent nanoparticle P-selectin antagonist with anti-inflammatory effects in allergic airway disease. *The FASEB Journal* **17**, 2296–2298 (2003).

58. Mehanna, E. A., Attizzani, G. F., Kyono, H., Hake, M. & Bezerra, H. G. Assessment of coronary stent by optical coherence tomography, methodology and definitions. *Int J Cardiovasc Imaging* **27**, 259 (2011).

59. Mancuso, J. J. *et al.* Intravascular optical coherence tomography light scattering artifacts: merry-go-rounding, blooming, and ghost struts. *J Biomed Opt* **19**, 126017 (2014).

60. Yao, L., Pan, J., Setiadi, H., Patel, K. D. & McEver, R. P. Interleukin 4 or oncostatin M induces a prolonged increase in P-selectin mRNA and protein in human endothelial cells. *Journal of Experimental Medicine* **184**, 81–92 (1996).

61. Misugi, E., Tojo, S. J., Yasuda, T., Kurata, Y. & Morooka, S. Increased Plasma P-Selectin Induced by Intravenous Administration of Endotoxin in Rats. *Biochem Biophys Res Commun* **246**, 414–417 (1998).

62. Fang, H. *et al.* The severity of LPS induced inflammatory injury is negatively associated with the functional liver mass after LPS injection in rat model. *J Inflamm (Lond)* **15**, (2018).

63. Longmire, M., Choyke, P. L. & Kobayashi, H. Clearance Properties of Nano-sized Particles and Molecules as Imaging Agents: Considerations and Caveats. *Nanomedicine (Lond)* **3**, 703 (2008).

64. De Jong, W. H. *et al.* Particle size-dependent organ distribution of gold nanoparticles after intravenous administration. *Biomaterials* **29**, 1912–1919 (2008).

65. Lesina, A. C., Berini, P., Vaccari, A. & Ramunno, L. On the convergence and accuracy of the FDTD method for nanoplasmonics. *Optics Express, Vol. 23, Issue 8, pp. 10481-10497* **23**, 10481–10497 (2015).

66. Vial, A., Laroche, T., Dridi, M. & Le Cunff, L. A new model of dispersion for metals leading to a more accurate modeling of plasmonic structures using the FDTD method. *Appl Phys A Mater Sci Process* **103**, 849–853 (2011).

Acknowledgements:

The authors would like to thank Dr. XiaoLing Zhao for the many histological samples she prepared and scanned, as well as Sabaa Rashid for the focused-ion beam transmission electron microscopy milling and helium ion microscopy images. The authors would also like to thank Dr. Yun Liu and Dr. Jianqun Wang for transmission and scanning electron microscopy imaging of many samples. Finally, the authors would also like to thank Dr. Linda Kempe and Dr. Emmanuel Yumvihoze for their rapid and careful processing of tissue, and ICP-MS analysis for the biodistribution assay. A.J.S. acknowledges funding support from Canada Research Chairs (950-230754), NSERC Discovery Grant (RGPIN- 2021-03387), and UOHI Precision Medicine Pilot Fund.

Author contributions:

N.D.C. performed all AuSC/AuNP syntheses, characterization, *in vitro* IV-OCT experiments, and evaluated targeting performance of AuSC@$(13FS)_2$. N.D.C performed all chemical syntheses with support from A.A.T. All FDTD simulations were performed by J.S.J.B, J.T, and L.R. FIB-TEM and HIM was performed by J.W. and P.B. N.D.C and A.K. developed the rat inflammation model and prepared histological samples. N.D.C and A.J.S. performed all *in vivo* IV-OCT and *in vivo* biodistribution analysis experiments, with support from B.H. N.D.C. and S.N. performed mouse serum stability studies. N.D.C performed all statistical analyses. N.D.C, A.J.S, and B.H. conceived of experiments with support from L.R. and E.H. N.D.C. and A.J.S. co-wrote the paper, and all authors edited the work and provided input.

Competing interests:

N.D.C. and A.J.S. have a patent application on the synthesis and application of metal nanoclusters for biomedical imaging (PCT/CA2023/05005).